

Article

Probabilistic Analysis of Ground Surface Settlement of Excavation Considering Spatial Variable Modified Cam-Clay Model Parameters

Hao Cheng ^{1,2}, Hui Chen ², Hanying Jia ³, Shu Zhang ^{2,*}  and Xiao Liu ² ¹ China Railway Siyuan Survey and Design Group Co., Ltd., Wuhan 430063, China² Badong National Observation and Research Station of Geohazards, China University of Geosciences, Wuhan 430074, China³ China Energy Engineering Group Hunan Electric Power Design Institute Co., Ltd., Changsha 410007, China

* Correspondence: szhang@cug.edu.cn

Abstract: The modified Cam-clay model (MCC model) is capable of representing the consolidation process of the soil under a complex stress path and thus is extensively adopted in the numerical analysis of excavation engineering. For reliability problems of ground surface settlement of excavation, minimal attention has been paid to investigating the effect of spatial variable MCC model parameters on the settlement during the staged construction of the excavation. Based on laboratory tests and sensitivity analysis, this study launched the probabilistic transient hydro-mechanical coupling analysis of excavation settlement considering spatial variable deformation parameters (λ and κ) using an MCS-FORM hybrid approach. The results show that: (1) Both the deformation parameters have a positive relationship with the settlement, and κ has a more significant effect than λ . (2) The observed maximum settlement and the location with maximum settlement follow a log-normal distribution. (3) An increasing COV of parameters leads to an enhanced surface settlement, expansion of the significant influence region, and decreased reliability. (4) The reliability index is greatly enhanced with the delimited controlled standard value of the surface settlement, H_{con} , and it decreases significantly at the preliminary stage and then decreases progressively until stable during excavating. Overall, adopting the deterministic analysis without considering the spatial variability of MCC parameters leads to underestimating the risk due to the settlement and the significant influence region.

Keywords: modified cam-clay model; reliability; ground surface settlement; excavation



Citation: Cheng, H.; Chen, H.; Jia, H.; Zhang, S.; Liu, X. Probabilistic Analysis of Ground Surface Settlement of Excavation Considering Spatial Variable Modified Cam-Clay Model Parameters. *Appl. Sci.* **2022**, *12*, 9411. <https://doi.org/10.3390/app12199411>

Academic Editor: Ricardo Castedo

Received: 17 August 2022

Accepted: 18 September 2022

Published: 20 September 2022

Publisher's Note: MDPI stays neutral with regard to jurisdictional claims in published maps and institutional affiliations.



Copyright: © 2022 by the authors. Licensee MDPI, Basel, Switzerland. This article is an open access article distributed under the terms and conditions of the Creative Commons Attribution (CC BY) license (<https://creativecommons.org/licenses/by/4.0/>).

1. Introduction

As urbanization accelerates, the construction of large and complex underground infrastructure has necessitated launching a series of excavations [1,2]. Within the excavation depth, when encountering an aquifer, it is commonly required to set up a seepage barrier curtain to drain the underground water preliminarily, then to brace and excavate, and a staged construction is also necessary. During this process, the increased effective stress in the soil within the groundwater depression cone contributes to soil compression, manifested as a soil settlement [3]. It typically leads to a series of safety threats to the surrounding buildings, thus affecting the urban economy and human safety significantly. To some extent, under the premise of ensuring its stability, the deformation control of pits and the influence on the surrounding environment have become crucial issues of excavations [4]. Hence, it has become a priority of geotechnical engineers to accurately evaluate the patterns of ground settlement variations during staged excavation, which is of great engineering significance and research value.

Traditionally, settlement induced by soil consolidation has been one of the most classic problems explored in geotechnics [5], and there has been a dramatic increase in simple theoretical solutions [6,7]. The settlement caused by excavation is a comprehensive geotechnical

engineering challenge involving a series of problems in soil mechanics such as strength, stability, deformation, groundwater seepage, etc. Simple theoretical solutions often fail to comprehensively express the effects of numerous parameters, thus having limited applications [8]. For the above reasons, numerous studies have investigated the deformation caused by excavation construction based on the empirical method with statistical analysis of a significant amount of measured data [9–13]. However, it has the shortcoming of disregarding the discrepancies between different stratigraphic conditions and soil mechanical properties. Thus the findings are not convincing.

The numerical analysis solutions represented by the finite element method (FEM), comparatively, enable to consider not only the coupling effect of a variety of factors but also the sophisticated nonlinear mechanical properties of the soil, thus becoming an effective way to address the problem and being applied extensively in practical engineering [14–18]. It confirmed the critical role played by the constitution model of the geotechnical material employed in numerical simulation [19,20]. The modified Cam-clay (MCC) model can reproduce the consolidation process of the soil under a complex stress path of repeated loading and unloading [21–23]. It is recognized by many studies as particularly applicable to deformation problems such as excavation [24] and has developed productive results [25–30]. However, the deterministic approach treats geotechnical materials as homogeneous and employs invariant geotechnical parameters obtained by limited time-consuming tests or analogy methods, which is inconsistent with the actual situation.

While the geotechnical parameters, including MCC model parameters, are characterized by spatial variability due to depositional conditions, stress history, weathering, and other geological effects [31–33]. Relatively, the probabilistic analysis of the excavation provides a solution that considers the uncertainty of geotechnical parameters [34,35]. Goh et al. [36] evaluated the stability of basement uplift in clay pits using a reliability index-based approach. Luo and DAS [37] proposed a simplified framework system for assessing the probability of surface displacement failure due to foundation excavation. Zhang et al. [38] investigated the reliability of ground surface settlement behind excavations employing a first-order reliability method (FORM) implemented with a variance reduction technique while considering spatial variable shear strength and stiffness of soft clay of the Harding small strain (HSS) model. Concerning the application of the MCC model in reliability analysis, Lu et al. [39] investigated the effect of uncertainty of an individual parameter on one-dimensional foundation consolidation and settlement problems based on the Monte Carlo simulation (MCS) method combined employing the stochastic finite element method (SFEM). Savvides and Papadrakakis [40] investigated the effect of the uncertainty of parameters on the probability of foundation settlement under inclined loading. There are two issues in the current study. (1) Although numerous studies have focused on the spatial variable stiffness and strength of soils, minimal attention, so far, has been paid to investigating the effect of the spatial variable MCC model parameters on the ground surface settlement of excavation. (2) Despite the deformation of the excavation being inseparable from the seepage process, the current probabilistic analysis emphasized mainly static stress analysis, with little research on the transient hydro-mechanical coupling problems during draining.

Given the above issues, the novelties of this study lie in the following aspects. Firstly, it focused on the effect of spatial variability of deformation parameters when introducing the MCC model in excavation settlement problems. Secondly, this study particularly investigated the time-dependent deformation and reliability of ground surface settlement of the entire draining, bracing, and excavating process since the staged construction style. The statistics of surface settlement, region with the maximum settlement and the reliability of the excavation were examined. A further study of the effect of the controlled standard settlement threshold and coefficient of variation (COV) of the parameters on the results was also discussed. The framework and findings will contribute to an increased understanding of reliability-based foundation excavation design and control.

2. Basic Theory

2.1. MCC Model

The MCC model is a relatively well-developed and extensively applicable elastic-plastic constitutive model in geotechnics. Roscoe [22] improved the Cambridge model based on the critical state theory by modifying the flow rules with the hardening parameter, which can effectively reflect the soil's bulk compression and rebound properties. The model captures the hardening and softening of the soil by the size of the critical state surface.

In p - q space, the yield surface of the MCC model presents as an elliptical curve, as shown in Figure 1. It can be denoted as

$$q^2 + M^2 p(p + p_c) = 0 \tag{1}$$

where p denotes the mean effective pressure, q denotes the deviatoric stress determines the size of the yield surface, p_c denotes the value of the consolidation pressure, and M is the slope of the critical state line (CSL) that passes through the origin. It is assumed that the soil hardening and softening are only related to the plastic volumetric strain, which dominates the size of the plastic yield surface. When plastic volumetric contraction occurs, the yield surface becomes larger, and the soil stress falls on the left side of the CSL ($q < Mp$), resulting in softening of the soil. Otherwise, when plastic volumetric expansion occurs, the yield surface reduces, and the soil stress falls on the right side of the CSL ($q > Mp$), resulting in the hardening of the soil.

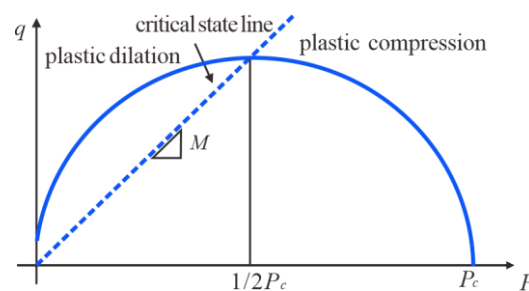


Figure 1. Yield surfaces in the MCC model.

As the plastic volume changing, the updated consolidation pressure p_c^N can be computed using the following equation.

$$p_c^N = p_c \left(1 + \Delta \epsilon_p^p \frac{\nu}{\lambda - \kappa} \right) \tag{2}$$

where $\Delta \epsilon_p^p$ denotes the increment of plastic volumetric strain, ν is the specific volume, λ is the slope of the normal consolidation line, and κ is the slope of an elastic swelling line for an unloading-reloading excursion.

The MCC model includes eight parameters: (1) rebound index, κ ; (2) compression index, λ ; (3) critical stress ratio, M ; (4) Poisson's ratio, ν ; (5) β , a parameter controlling the shape of the yield surface, generally taken as 1; (6) void ratio e_1 on the NCL line when $p = 1$, which is used to obtain the parameter α_0 that determines the location of initial yield surface; (7) initial void ratio e_0 , which represents the current compact state of the soil; (8) initial stress p_0 , which can be calculated by the ground stress balance. Among them, the first four parameters (λ , κ , M , and ν) are directly associated with the deformation. The parameters β and e_1 determine the location and shape of the initial yield surface. The parameters e_0 and p_0 determine the initial state of the soil conjointly but have no impact on the variation of the void ratio, i.e., the volumetric strain. Besides, the preconsolidation pressure p_c defines the size of the yield surface [41].

Generally, λ , κ and M are regarded as the three primary parameters for the MCC model. The former two parameters are ideally obtained from the isotropically loading-

unloading triaxial test. However, they can be derived in terms of empirical relations (Equations (3) and (4)) with compression index (C_c) and swelling coefficient (C_s) obtained by an oedometer test, which will be presented in the following section. M can be derived according to the empirical relation (Equation (5)) with the effective friction angle, ϕ' , obtained from a triaxial compression test [42].

$$\lambda = C_c / \ln(10) \quad (3)$$

$$\kappa \approx C_s / \ln(10) \quad (4)$$

$$M = 6 \sin \phi' / (3 - \sin \phi') \quad (5)$$

2.2. Random Field Theory

Random field theory enables the characterization of the randomness characteristics of geotechnical parameters at arbitrary spatial locations and the correlation characteristics in the spatial variability of soil parameters [43]. In particular, the randomness characteristics are generally depicted by the coefficient of variation, while the theoretical autocorrelation function depicts the correlation characteristics. Some of the most frequent autocorrelation functions are exponential, exponential cosine, and trigonometric autocorrelation functions [44]. This study denoted the autocorrelation functions employing an exponential autocorrelation function in the form of:

$$\rho(\tau_x, \tau_z) = \exp \left[-2 \left(\frac{|\tau_x|}{\theta_x} + \frac{|\tau_z|}{\theta_z} \right) \right] \quad (6)$$

where $\rho(\tau_x, \tau_z)$ is the correlation function, indicating the correlation between the two points, with the range of $0 \leq \rho \leq 1$; θ_x and θ_z are the scales of fluctuation (m) in the x and z directions, respectively, indicating the spatial correlation scales of the two directions. If θ_x is inequivalent to θ_z , it indicates an anisotropic correlation structure.

3. Materials and Methods

3.1. A Case Study of Excavation

3.1.1. Numerical Model, Boundary Conditions and Calculation Conditions

A metro excavation project in Hangzhou, Zhejiang Province of China, was chosen as the research object of this study. According to the borehole data of geotechnical engineering investigation implemented by China Railway Siyuan Survey and Design Group Co., Ltd. (CRSSDGC) [45], a typical drill core representing the stratigraphic profile of the soil layer of the excavation is shown in Figure 2. The lithology of the soil is mainly silt, combined with thin layers (thickness less than 5 m) of clayey silt, miscellaneous fill, and pebble soil. In this study, the spatial variability of soil deformation parameters requires massive computations. Thus it would increase the computational effort if all these thin soil layers are manifested. Moreover, if the spatial variability of parameters of all the soil layers is considered, a curse of dimensionality may arise. Therefore, we generalized the soil layers into a homogeneous and isotropic silt layer to simplify the computation.

Moreover, the buried depth of phreatic water level by drilling during the investigation was typically 0~2.6 m [45]. Hence, the seepage path of groundwater was increased by setting up a suspended seepage barrier curtain during excavation, combined with draining in the pit, enabling the groundwater level to be dropped in the pit while the head loss outside the pit was reduced.

Given the regularity of the planar shape of the pit, this study established a 2D planar finite element model for analysis, as shown in Figure 3. The size of the pit calculation model is 422 m \times 50 m, with an excavation width of 22 m and a depth of 12 m. The excavation was braced by a suspended seepage barrier curtain (also known as an underground diaphragm wall), reinforced concrete support of 1000 mm \times 1000 mm, and two inner steel braces with a diameter of 800 mm and a spacing of 4 m between the braces.




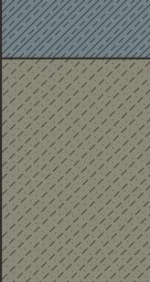



Soil profile	Bottom height	Chronostratigraphic code	Soil sample	Stratigraphic information
	-2.5m	Q_4^{m1}		Miscellaneous fill
	-5.6m	Q_4^{3a1+m}		Silt
	-7.4m	Q_4^{3m}		Clayey silt
	-21.5m	Q_4^{3a1+m}		Silt
	-25.1m	Q_4^{1a1+m}		Clayey silt
	-40.8m	Q_4^{3a1+m}		Silt
	-45.3m	Q_4^{1a1+m}		Clayey silt
	-48m	Q_4^{1a1+m}		Pebble soil

Figure 2. A typical drill core in the study area.

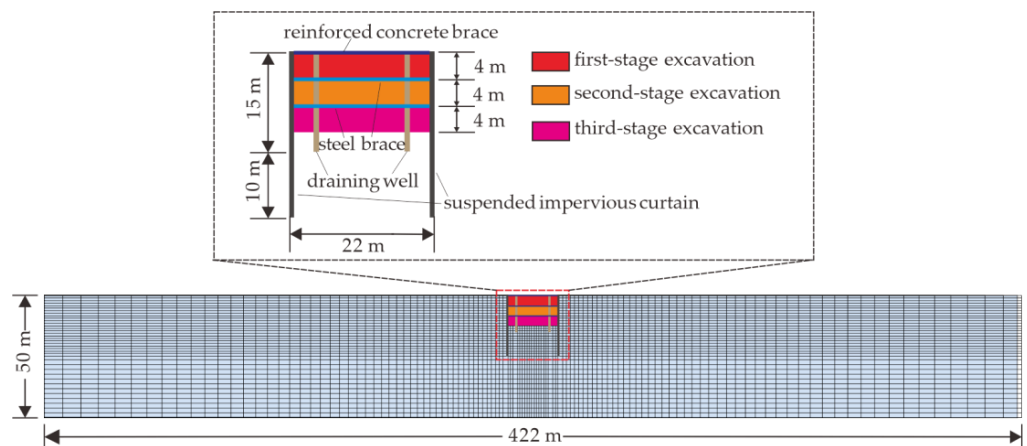


Figure 3. The excavation model adopted in the finite element analysis.

In the FEM analysis, a numerical model was developed. It employed the CPE4P (4-node plane strain quadrilateral) elements for soil, the B21 (2-node linear beam in a plane) elements for the reinforced concrete support and steel support, and the CPE4 (4-node bilinear plane strain quadrilateral) elements for the suspended seepage curtain. The grid size near the pit was set as 1 m × 1 m, and the grid size near the horizontal boundary of the model was 5 m × 1 m. Thereby, the model was divided into a total of 4682 elements and 14,724 nodes.

The top of the model was a free boundary. Both horizontal and vertical displacement at the bottom boundary were restricted. The shearing behavior of the soil on the lateral boundaries [46–48] was not considered due to the sufficient distance from the excavation.

However, the horizontal displacement of the lateral boundaries was restricted, but the vertical movement was allowed for safety considerations. The horizontal displacement of the sidewalls of the drainage well was also restricted.

A phreatic water boundary condition on the ground surface was set on both sides of the model to simulate the distal seepage recharge. Considering the significance of the water level to the settlement [49], the phreatic water level was set to the highest level of 0 m based on the survey observation to consider the most unfavorable scenario with the maximum drawdown and water level difference inside and outside the pit.

Both sides of the drainage wells were fixed-head boundaries to simulate the draining process. The bracing exertion and soil excavation were simulated using the raw and dead unit method.

Foundation pit draining and excavation is a process of joint action of stress field and seepage field, involving soil stress equilibrium, pore water seepage, and the coupling action between them. This study employed the seepage and stress coupling module of the ABAQUS code [41] to perform a transient flow-solid coupling analysis of the draining and excavation process based on the total pore pressure variation of the soil and the effective stress method.

Controlling the deformation of the excavation, a staged construction process in terms of draining, bracing, and excavating is demanded to be elaborated. A specific work process in this study is as follows, which only covers the main steps in the simulation.

Stage I: perform the first-stage draining, dropping from the surface (0 m) to 1 m below the first-stage excavation surface (−4 m). Then excavate 0.5 m deep downward to activate the first-stage reinforced concrete support unit, continuing to excavate 3.5 m in depth. The entire process lasted ten days.

Stage II: perform the second-stage draining, dropping from −5 m to 1 m below the second-stage excavation surface (−8 m). Then excavate 0.5 m deep downward to activate the second-stage reinforced concrete brace unit, continuing to excavate 3.5 m in depth. The entire process lasted ten days.

Stage III: perform the third-stage draining, dropping from −9 m to 1 m below the third-stage excavation surface (−12 m). Then excavate 0.5 m deep downward to activate the third-stage reinforced concrete brace unit, continuing to excavate 3.5 m in depth to the designated elevation. The entire process lasted ten days.

3.1.2. Adopted Parameters for FEM Analysis

According to the borehole data obtained by the geotechnical engineering investigation [45], the soils predominantly distributed in the study area are grayish-yellow to greenish-gray clayey silt, which is slightly dense and has high water content. The oedometer test with several unloading excursions was performed to obtain the parameters (C_c and C_s) of the MCC model. The tests were launched in a triplex WG-type high-pressure consolidator, as shown in Figure 4. The scalped standard soil specimens of 61.8 mm in diameter and 20 mm in height were prepared from the in-situ samples obtained from thin-walled soil extractors during drilling. A total of three sets of specimens were prepared and placed in the retaining ring of the consolidation vessel. The test was performed in a step-by-step loading mode, and each load level was consolidated for 24 h until the total deformation of the specimen was less than 0.01 mm per hour, and the loading and unloading ratings are shown in Figure 4. All the sampling and launching procedures of the test were referred to the Standard geotechnical testing method (GB/T50123-2019) [50].

The e - $\lg p$ curves obtained from three sets of parallel oedometer tests are shown in Figure 5. The compression index C_c and the rebound index C_s of the uniaxial oedometer test were then obtained according to the following equation:

$$C_c \text{ or } C_s = \frac{e_i - e_{i+1}}{\lg p_{i+1} - \lg p_i} \quad (7)$$

$$e_i = e_0 - (1 + e_0) \frac{\sum \Delta h_i}{h_0} \tag{8}$$

where e_i is the void ratio at a certain level of pressure p_i ; e_0 is the initial void ratio; $\sum \Delta h_i$ is the total deformation height of the specimen at a certain pressure level, and h_0 is the initial height of the specimen. As marked in Figure 5, the C_c of sample 3# is denoted as the slope of the straight line segment of the compression curve, which is the tangent of the reloading curve. The C_s is the slope of the line between the endpoint of the unloading curve and the intersection of the reloading and unloading curves. Then the average value of the three samples was employed for the final result. The results of C_c and C_s are also listed in Figure 5. Then according to Equations (3) and (4), λ and κ can be derived from C_c and C_s . M can be obtained from the triaxial compression test performed by CRSSDGC [45] on the basis of Equation (5).

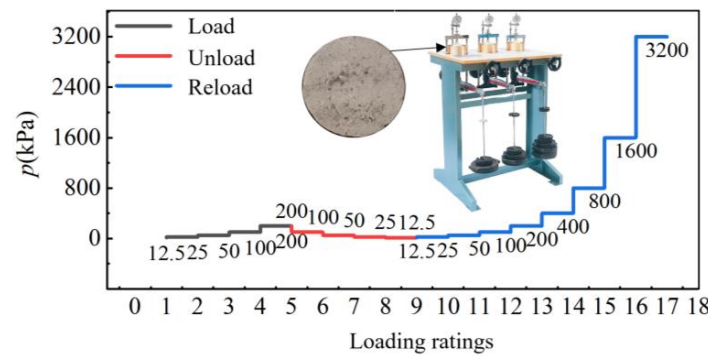


Figure 4. The apparatus and loading ratings of the oedometer test.

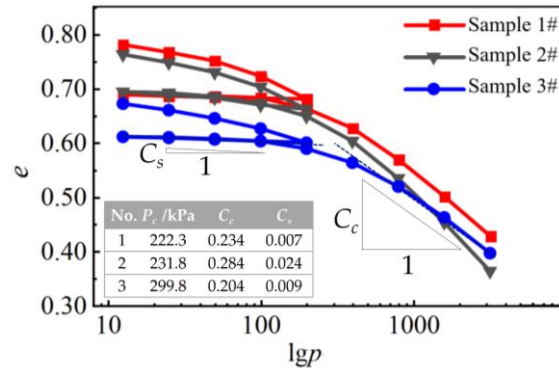


Figure 5. The e - $lg p$ curves obtained from the oedometer test.

Besides, the geotechnical investigation report also provided the physical and mechanical properties of the soil based on comprehensive laboratory and field tests. The parameters adopted in the deterministic simulation analysis are shown in Table 1. Specifically, the physical parameters (i.e., void ratio, dry density) were obtained from conventional laboratory tests. The lateral pressure coefficient (K_0) was obtained according to the K_0 oedometer test, and the Poisson’s ratio (ν) can be derived from the correlation with K_0 as $\nu = K_0 / (1 + K_0)$. The saturated hydraulic conductivity (K_s) was obtained from the field pumping test.

Table 1. Physical and mechanical parameters of silt for the excavation.

Void Ratio	Dry Density	Saturated Hydraulic Conductivity	Poisson’s Ratio	Lateral Pressure Coefficient	MCC Model Parameters		
e_0	ρ_d	K_s	ν	K_0	λ	κ	M
-	kg/m ³	m/s	-	-	-	-	-
0.78	1700	1.82×10^{-6}	0.28	0.39	0.106	0.00362	1.113

Regardless of the permeability, the mechanical parameters of the retaining structure of the excavation are shown in Table 2.

Table 2. The mechanical parameters of the retaining structure of the excavation.

Retaining Structure	Density/kg·m ⁻³	Poisson’s Ratio	Elastic Modulus/GPa
Underground continuous wall	2400	0.15	31.5
Reinforced concrete	2400	0.15	30.0
Steel frame	7800	0.20	210

With regard to probabilistic analysis, it has been recognized that most geotechnical parameters in practical engineering are subject to log-normal distribution [51]. Baroth [52] has also suggested that the MCC model parameters of soils can be randomly sampled according to a log-normal distribution. Concerning spatial correlation, the random field theory proposed by Vanmarcke [53] was employed in this study. This study employed an exponential function to simulate the spatial autocorrelation of the MCC model parameters, referring to the corresponding statistical results of typical soil layers in the Hangzhou area [54,55]. It took a horizontal correlation distance (δ_h) of 40 m, a vertical correlation distance (δ_v) of 0.5 m, and a coefficient of variation (COV) of 0.15 for all parameters. The mutual correlation between parameters was not considered herein.

3.2. Sensitivity Analysis Method of Deformation Parameters of Soil Based on Orthogonal Experimental Design

The orthogonal experimental design provides a simple but efficient way to study many factors and levels based on the orthogonal test table and mathematical statistics [56,57]. The orthogonal test table reflects the balance of the considering factors and the uniformity of considering levels [58]. In an orthogonal test with multiple factors, $L_n(t^c)$ is the representation of the orthogonal table, in which L denotes the code of the orthogonal table; n is the number of orthogonal table rows, denoting the number of conducted tests; t denotes the number of levels and c denotes the number of factors.

To examine the parameters with the most significant effect on the deformation of the excavation, four deformation-related MCC parameters (λ , κ , M , and ν) were selected to conduct the sensitivity analysis in this section. Therefore, an orthogonal test table with four factors and three levels was employed and presented in Table 3. According to Section 3.1.2, the MCC parameters were assumed to be log-normally distributed, and ν was often assumed to be normally distributed [59]. Given the representativeness of the levels taken for each factor, the MCC parameters were taken for three levels, i.e., $e^{\mu-2.5\sigma}$, e^μ , and $e^{\mu+2.5\sigma}$, while ν values were taken for $\mu - 2.5\sigma$, μ and $\mu + 2.5\sigma$, as presented in Table 4.

Table 3. $L_9(3^4)$ orthogonal test table.

Test No.	Factors			
	λ	κ	M	ν
1	1	1	1	1
2	1	2	2	2
3	1	3	3	3
4	2	1	2	3
5	2	2	3	1
6	2	3	1	2
7	3	1	3	2
8	3	2	1	3
9	3	3	2	1

The statistical analysis methods of orthogonal experimental design include the analysis of extreme variance and analysis of variance. Employing the former, it calculates each factor’s mean value and extreme difference at each level. It plots the trend of factors and

assessment indexes, thus distinguishing the order of influence of each factor on assessment indexes [60].

Table 4. Four factors and the corresponding levels in the study.

Levels	Factors			
	λ	κ	M	v
1	0.0954	0.00226	0.696	0.24
2	0.106	0.00362	1.113	0.3
3	0.117	0.00498	1.530	0.33

3.3. Deformation Analysis Method of Excavation Based on Random Field Theory

3.3.1. Method and Steps of Random Field Simulation

In this study, taking the log-normal random field of the parameter i as an example, a brief description of the method and steps of the midpoint method based on the Cholesky decomposition and Latin hypercube sample (LHS) [61] is presented as follows:

- (1) LHS was adopted to generate a random sample matrix ζ with independent standard normal distribution.
- (2) For the standard normal equivalent cross-correlation matrix $R_0 = (\rho_{0ij})_{nm}$, the Cholesky decomposition $L_1 L_1^T = R_0$ was performed to obtain the lower triangular matrix L_1 . Multiply the transposed matrix L_1^T with the sample matrix ζ so as to obtain the associated standard normal distribution sample matrix $\chi^D = \zeta L_1^T$.
- (3) With regard to the autocorrelation coefficient matrix $\sum_{\chi\chi}^G$, the Cholesky decomposition $L_2 L_2^T = \sum_{\chi\chi}^G$ was performed to obtain the lower triangular matrix L_2 , thereby obtaining the correlated standard Gaussian random field by the following equation:

$$H_i^D(x, y) = L_2 \cdot \chi^D = L_2 \cdot \zeta \cdot L_1^T \tag{9}$$

- (4) The correlated standard Gaussian random field $H_i^D(x, y)$ was converted to the correlated non-Gaussian random field by an equal probability conversion method as the following equation:

$$H_i(x, y) = G_i^{-1} \left\{ \varphi \left[H_i^D(x, y) \right] \right\} \tag{10}$$

where $G_i^{-1}(\cdot)$ is the inverse function of the marginal cumulative distribution of the non-Gaussian distribution and $\varphi(\cdot)$ is the cumulative distribution function of the standard normal distribution.

- (5) Taking the exponential correlated standard Gaussian random field, the correlated log-normal random field of the parameter was obtained employing the equation:

$$H_i(x, y) = \exp \left(\mu_{\ln i} + \sigma_{\ln i} \cdot H_i^D(x, y) \right) \tag{11}$$

where $\mu_{\ln i}$ and $\sigma_{\ln i}$ denote the mean and standard deviation of normally distributed variable $\ln i$.

A couple of points should be stated here: (1) the purpose of LHS is to improve the representativeness of the random sample; (2) the above random parameters require a standard normal distribution, otherwise it is required to be transformed in advance.

3.3.2. Method and Steps of SFEM Analysis

The stochastic finite element method was employed in this study to conduct the excavation surface deformation analysis, and the main steps are as follows.

- (1) Establish a numerical calculation model for excavation based on the ABAQUS code [38].
- (2) Extract the center coordinates of each element of the numerical model based on self-defined Python code.

- (3) Simulate the random field based on the center point coordinates extracted in (2) using the Cholesky decomposition method.
- (4) Establish the uncertainty model for the excavation in a batch using the simulated random field, perform the seepage stress coupling analysis, and document and save the results of each stochastic simulation for analysis.

3.4. Reliability Analysis Method for Excavation Settlement

Among the reliability analysis method, FORM, based on the gradient approach, estimates the probability of failure by identifying the most likely failure point in the normalized space. Its main drawback is that the derivative of the function is required to be computed to obtain the basic random variable, but it is currently impractical to quantify its derivative [62]. Comparatively, the MCS employs a random sampling method based on statistical theory to extract a set of values that satisfy the probability distribution of variables for the performance function. Multiple values of evaluation indicators under the sampling values and the probability distribution of evaluation indicators were obtained for reliability analysis. Although the results are typically considered more reliable, it has a shortcoming in terms of computational efficiency and cost [63]. Given that, this study adopted the MCS-FORM hybrid method to carry out the pit deformation reliability analysis. It employs MCS to derive the dimensionless moments of the functional function and then estimates the failure probability using the derived moments using FORM. This method takes full advantage of the effectiveness of MCS in a random sampling of geotechnical parameters and the efficiency of FORM in estimating reliability [61].

Firstly, the performance function G for the ground settlement reliability analysis of the excavation was defined as:

$$G = H_{con} - H_{sim} \quad (12)$$

where, H_{con} is the subjective defined the controlled standard value of surface settlement of excavation, which is governed by the grade of the construction and the area where the construction is located, and H_{sim} is the simulated surface settlement. If $G > 0$, the surface settlement on the outside of the pit is considered to be less than the control limit thus it is stable; otherwise, it is considered to be unstable if $G < 0$.

Based on the results of MCS, the statistics and dimensionless central moments of the function G are computed as follows:

$$\mu_G = \frac{1}{N} \sum_{i=1}^N G_i \quad (13)$$

$$\sigma_G = \left[\frac{1}{N} \sum_{i=1}^N (G_i - \mu_G)^2 \right]^{\frac{1}{2}} \quad (14)$$

$$m_{Gk} = \frac{\frac{1}{N} \sum_{i=1}^N (G_i - \mu_G)^k}{\sigma_G^k}, (k = 3, 4) \quad (15)$$

where, μ_G and σ_G denote the mean and standard deviation of G , G_i denotes the G value of the i th sample ($i = 1, 2, 3, \dots, N$), and m_{Gk} is k th order dimensionless central moment of G .

For the performance function G herein, if the first two moments are obtained and assumed to be normally distributed, the reliability index β can be computed as

$$\beta_G = \sigma_G / \mu_G \quad (16)$$

4. Results

4.1. Deterministic Ground Surface Settlement Analysis

The groundwater drawdown curves and ground surface settlement curves at various stages of draining and excavating for the excavation are depicted in Figures 6 and 7. As

shown in Figure 6, the groundwater level outside the excavation was higher than that inside for all draining stages, indicating that the suspended seepage barrier affected the hydraulic connection between the inner and outer sides, which thus controlled the surface settlement. As indicated in Figure 7, at each stage of the excavation draining and excavation, the surface settlement curve was groove-shaped with a single peak, which resembles the shape of the drawdown curve. The reason is that the draining increases the effective stress of the soil outside the pit, and the presence of head differences inside and outside the pit leads to the infiltration force downward in the active zone soil, resulting in a larger settlement. According to the data, the maximum surface settlement outside the excavation was 38.22 mm, 0.32% of the excavation depth. The location with the maximum settlement was 39.7 m from the center of the pit and 27.9 m from the seepage barrier, which was 2.33 times the excavation depth.

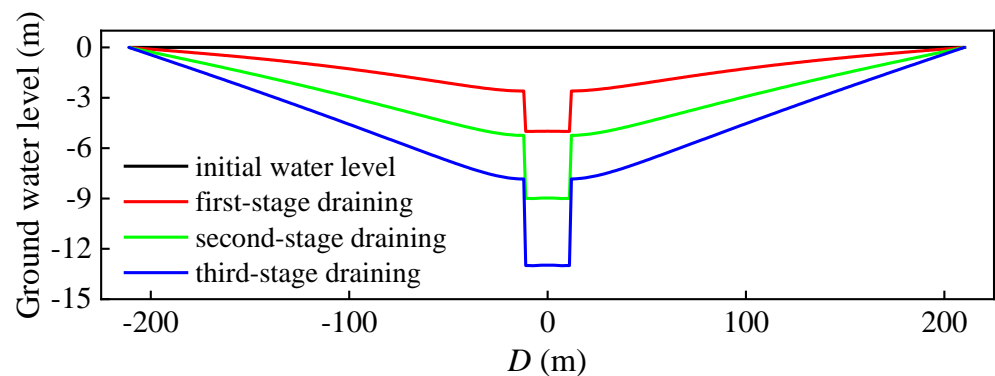


Figure 6. Drawdown curves of groundwater in the excavation for different construction stages.

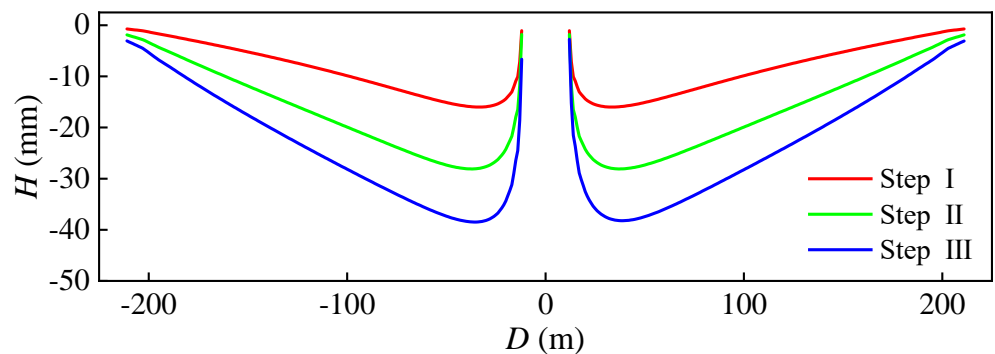


Figure 7. Surface settlement curves outside the excavation for different construction stages.

4.2. Sensitivity Analysis Method of Deformation Parameters

The obtained maximum ground settlements of the determined calculation model and extreme differences in the orthogonal tests are shown in Table 5. It indicates that for the finite element calculation model of the excavation in this study, the dominant order of the deformation parameters of the MCC model affecting the surface settlement was $\kappa > \lambda > \nu > M$.

It could also be confirmed by the mean values of settlements of different levels due to different parameters, as shown in Figure 8. With the increase of λ and κ , the settlement increased significantly, indicating that the surface settlement of the excavation was more sensitive to λ and κ . Relatively, for the variations of M and ν , the settlement only fluctuated in a slight range and was less sensitive to either of them, and no significant trend can be observed. In particular, the ground settlement was more sensitive to κ , as observed in comparative trend in Figure 9.

Table 5. The results of the orthogonal tests.

Test No.	Factors				Settlement (mm)
	λ	κ	M	ν	
1	0.0954	0.00226	0.696	0.24	29.34
2	0.0954	0.00362	1.113	0.3	39.21
3	0.0954	0.00498	1.530	0.32	54.64
4	0.106	0.00226	1.113	0.32	29.33
5	0.106	0.00362	1.530	0.24	34.48
6	0.106	0.00498	0.696	0.3	52.29
7	0.117	0.00226	1.530	0.3	39.76
8	0.117	0.00362	0.696	0.32	42.40
9	0.117	0.00498	1.113	0.24	52.41
K ₁	40.28	32.81	41.627	38.743	
K ₂	38.70	38.98	40.317	43.753	
K ₃	45.14	52.33	42.177	41.623	
Extreme difference	6.44	19.52	1.860	5.01	

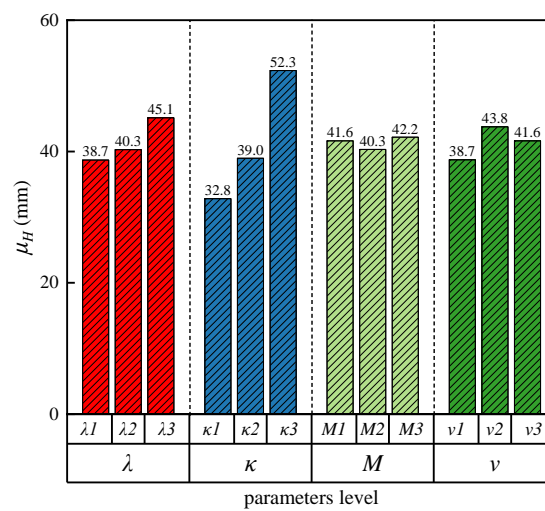


Figure 8. Mean values of surface settlement at different levels due to different parameters.

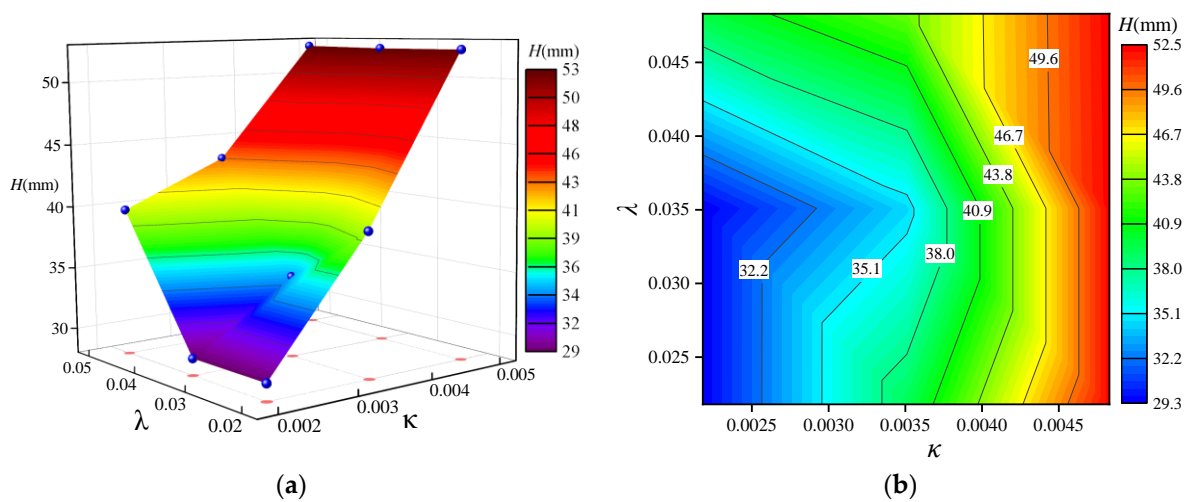


Figure 9. Effect of λ and κ on the ground settlement: (a) 3D view; (b) 2D planar view.

4.3. The Probabilistic Analysis

According to the sensitivity analysis results, the MCC model parameters λ and κ , which have the greatest influence on the settlement of the excavation, were selected to

establish a lognormal random field to carry out the probabilistic analysis. The same COV and scale of fluctuation were employed for each parameter, and the correlation between them was not considered.

Figure 10 depicts the derived relationship between the central moments of the G and the number of MCS runs. It indicated that m_{Gk} converges gradually with increasing the number of MCS runs, typically exceeding 900. Therefore, a total of 1000 uncertainty simulations were carried out for each scenario, and the statistics of the calculated results are as follows.

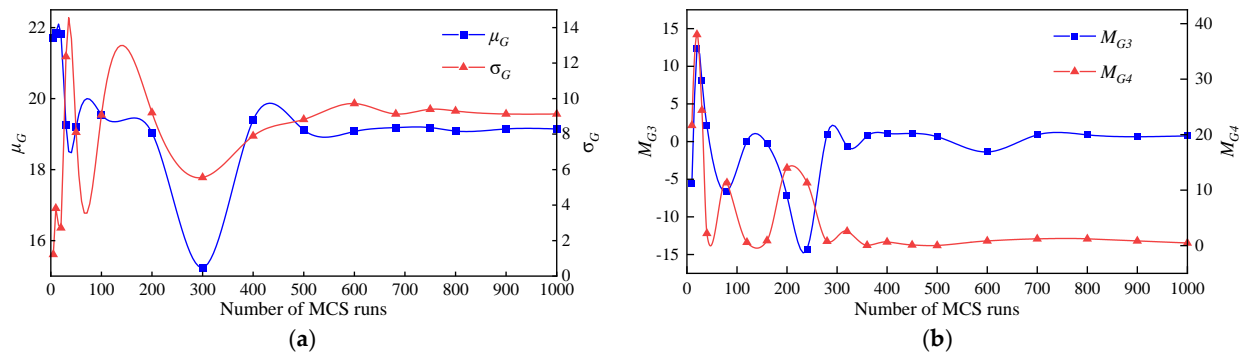


Figure 10. The convergence of the central moments of the performance function with the number of MCS runs: (a) mean and standard deviation; (b) third-order dimensionless central moment and fourth-order dimensionless central moment.

4.3.1. Statistics of Ground Surface Settlement

As depicted in Figure 11a, the ground surface settlement curve without considering the spatial variability of parameters is regular grooved, as shown by the red solid line in Figure 11a. While if the spatial variability is taken into account, each settlement curve computed from a certain realization is basically groove-shaped but bends and curls in a unique irregular way, as presents in the thin gray line in Figure 11a, which is utterly different from the former deterministic curve. These squiggly settlement curves computed from all the realizations cluster together and form a collection of settlement curves. It can be observed that the settlement curves of the two sides are not symmetrical, since the parameters of either side of the pit are typically non-symmetrical at all. The thick black dashed line herein envelopes the settlement curve collections and provides a full field-scale variation range that includes all possible deformations. Consequently, the variation of settlement can be implied that the spatial variability of the parameters is associated directly with the surface settlement at a certain location outside the seepage curtain. While in practical engineering, such variability has been verified and demonstrated by massive studies [1,29,30,33]. Therefore, it is required to be accounted for when performing settlement analysis.

For each D , it has a variation range of settlement corresponding to the curve collection, denoted by ΔH . The correlation between D and ΔH is illustrated in Figure 11b. It is squiggly downward groove, which is literally the reverse of the settlement curve. Overall, the particular location with a greater settlement is generally prone to having a larger ΔH . A closer inspection of ΔH shows it has a maximum value of 15.32 mm, which is 38.4% of the maximum settlement of determined analysis. In addition, the ΔH is quite insignificant for a great D , which is an unexpected outcome. It implies that the variation range of settlement is independent of variable parameters and is comparable with the deterministic results.

To identify the overall distribution of settlement data at different locations outside the curtain, six monitoring points ($D_1 \sim D_6$) were set in the model. The settlements obtained by all realizations at each monitoring point are represented by a violin plot, as shown in Figure 12. The settlements for each point have a bell-shaped distribution with only one peak. It depicted an overall trend that the variability of settlement decreases with increasing distance from the curtain (D'). A comparison of the median of H at each location outside

the curtain (in the black dashed line) with the deterministic settlement curve (in the red dashed line) indicated that it has an insignificant difference outside D_2 , but a significant difference within the range.

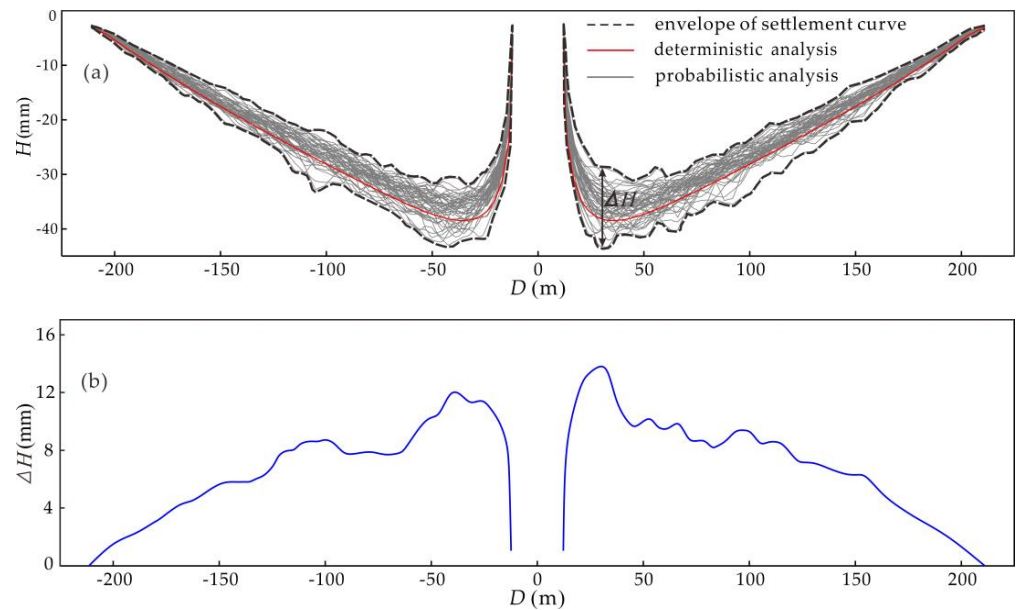


Figure 11. Ground surface settlement curves of determined and probabilistic analysis: (a) comparison of determined and probabilistic analysis; (b) correlation of variation range of settlement of probabilistic analysis (ΔH) and location (D).

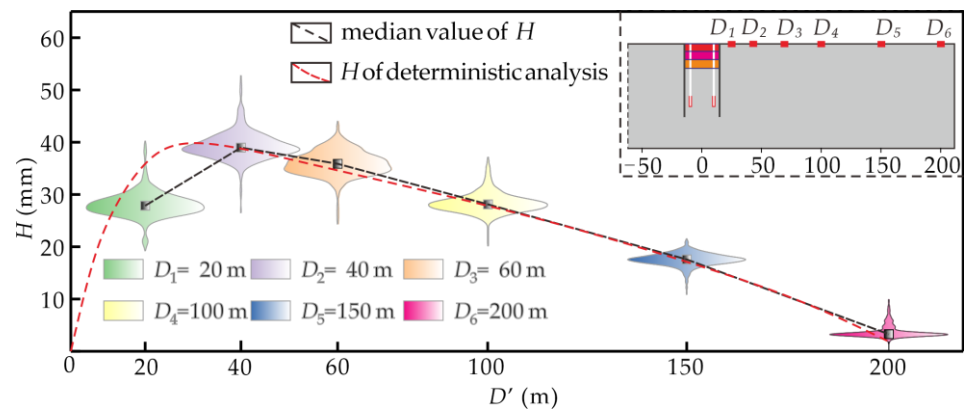


Figure 12. Violin plot of settlements of all the realizations at various locations.

The maximum settlement (H_m) and the distance of the maximum settlement location from the curtain (D'_m) for all 1000 realizations were statistically analyzed. Their histograms and probability density functions (PDFs) are shown in Figure 11. Following the Kolmogorov-Smirnov (K-S) test, H_m in Figure 13a was subjected to a log-normal distribution with a most frequent value within the interval of 40~42 mm, which was a bit larger than the deterministic analysis. It has a COV of 0.15, which was the same as the COV of the input random parameters λ and κ ($COV_{\lambda,\kappa}$). Meanwhile, D'_m in Figure 13b was distributed 5~110 m from the curtain and was subjected to a log-normal distribution. The most frequent value interval was 25~35 m, which was different from the results of the deterministic analysis (39.7 m). In a sense, D'_m signifies the region most significantly affected by settlement outside the excavation. It has a COV of 0.45, which was significantly larger than $COV_{\lambda,\kappa}$. This result demonstrated that the variability of D'_m was significantly greater than H_m . The location with the maximum settlement is typically the location with the most

severe deformation of buildings and transportation facilities, thus requiring attention in the practical construction.

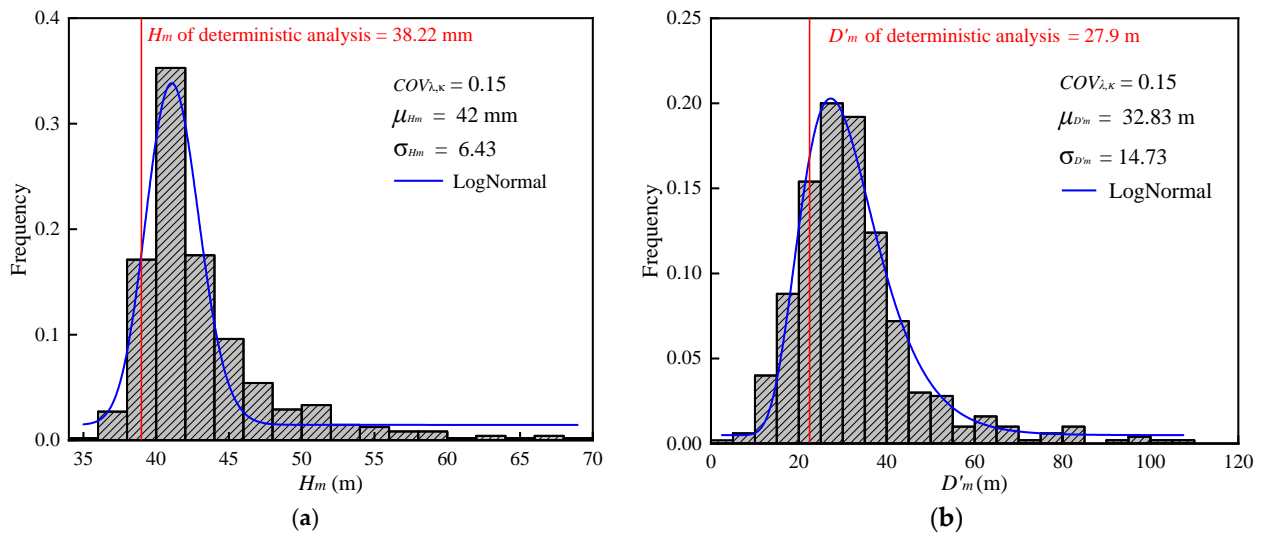


Figure 13. Histogram, fitting PDF curves, and statistics of H_m and D'_m : (a) H_m ; (b) D'_m .

4.3.2. Reliability of Ground Surface Settlement of the Excavation

As observed from Equation (10), the value of H_{con} contributed directly to the performance function G . As shown in Figure 14, the solid black line indicates the cumulative probability density curve of H_m from 1000 realizations. The red dashed line indicated that it has different guarantees within the control criteria under selected four individual values of H_{con} , i.e., 40 mm, 45 mm, 50 mm, and 60 mm. The H_m of the deterministic analysis was at the 0.32 quantiles of the cumulative probability density curve of H_m of the probabilistic analysis. It suggests that the risk of the excavation surface settlement assessed by deterministic analysis tends to be underestimated remarkably.

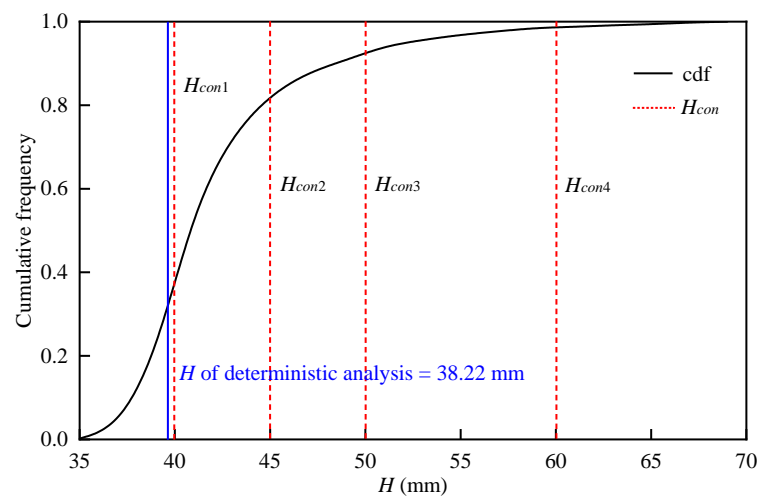


Figure 14. CDF of surface settlement with various control standard values.

As displayed in Figure 15, the comparison of the settlement control guarantee rate, R_g , and reliability index, β , increased significantly with H_{con} values. According to the related international standard [64], the reliability index for structures with irreversible deformation for a regular service limit state is 1.5. Given that the excavation is a temporary construction and the surface settlement is characterized by extendable deformation, the target β for surface settlement was delimited as 2.0 by referring to the prior studies combined with

economic guidelines. This reliability indicator was also recognized by excavation construction research [65]. Meanwhile, with the monitoring data of analogous excavations in the Hangzhou area (Table 6) and the actual excavating depth, H_{con} herein was delimited as 60 mm, thereby the R_g was 98.5%, and β was 2.7, meeting the requirements of engineering and construction.

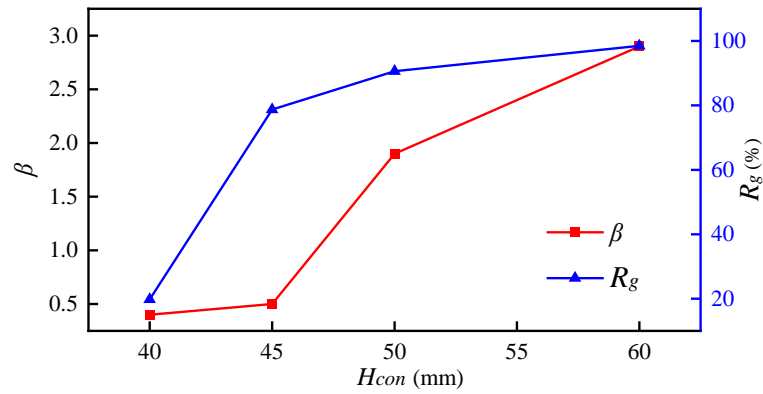


Figure 15. Effect of H_{con} on settlement control guarantee rate (R_g) and reliability index (β).

Table 6. Surface settlement values for similar excavation projects in the Hangzhou area.

No.	Reference	Depth of Excavation (m)	Monitored H_m (mm)
1	Shen [66]	24	85.65
		16.6	61.3
2	Wang [67]	14.8	88.0
		16.2	55.9
		16.5	71
		17~18.5	37.26
3	Qin [68]	16~18.5	79.68
		18~20	44.43
		16~17.2	69.41
4	Wei et al. [69]	33	67~88.61

Based on the above regulations, Figure 16 provides the temporal variation of reliability during the entire draining-bracing-excavating construction process. It demonstrates that no settlement was observed at the beginning of construction ($t = 0$). During Stage I and Stage II, the β decreases rapidly from 42.5 to 23.6 and then levels off during Stage II and Stage III. There are two possible explanations for this result. Firstly, due to the noticeable dropping of water level in the preliminary draining stage, the effect of ground consolidation and settlement was significant, and the reliability of surface settlement reduced rapidly. Secondly, with the step-by-step construction of the brace, the capability of resisting the deformation effect from draining and excavating was gradually enhanced. In particular, the pit tends to be stable as the entire formation of the third level of bracing structure.

4.3.3. Effect of $COV_{\lambda,\kappa}$ on Surface Settlement and Reliability of the Excavation

Figure 17 presents the correlation between the mean and COV of H_m at different construction stages with $COV_{\lambda,\kappa}$. As shown in Figure 15a, μ_{H_m} increases with the increase of $COV_{\lambda,\kappa}$ at each stage of construction. In terms of the incremental magnitude, Stage I was the least, followed by Stage II, and Stage III was the largest. An observation that COV_{H_m} increases with increasing $COV_{\lambda,\kappa}$ was also depicted in Figure 15b. It is also quite revealing that with the same $COV_{\lambda,\kappa}$, both μ_{H_m} and COV_{H_m} increased gradually with the construction of the excavation.

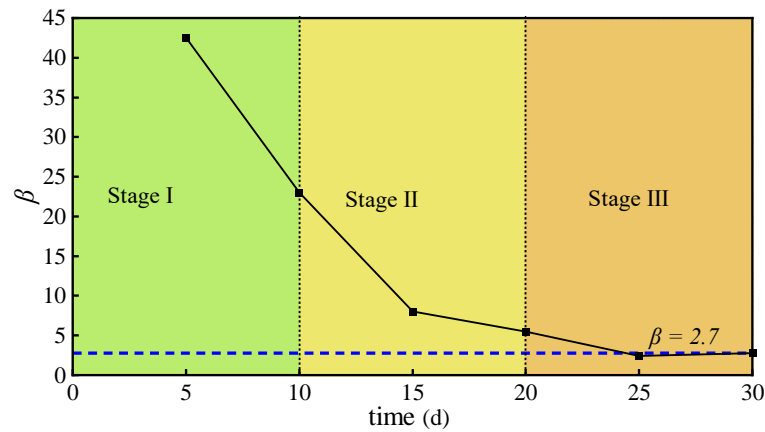


Figure 16. Time-varying reliability of ground surface settlement of the excavation.

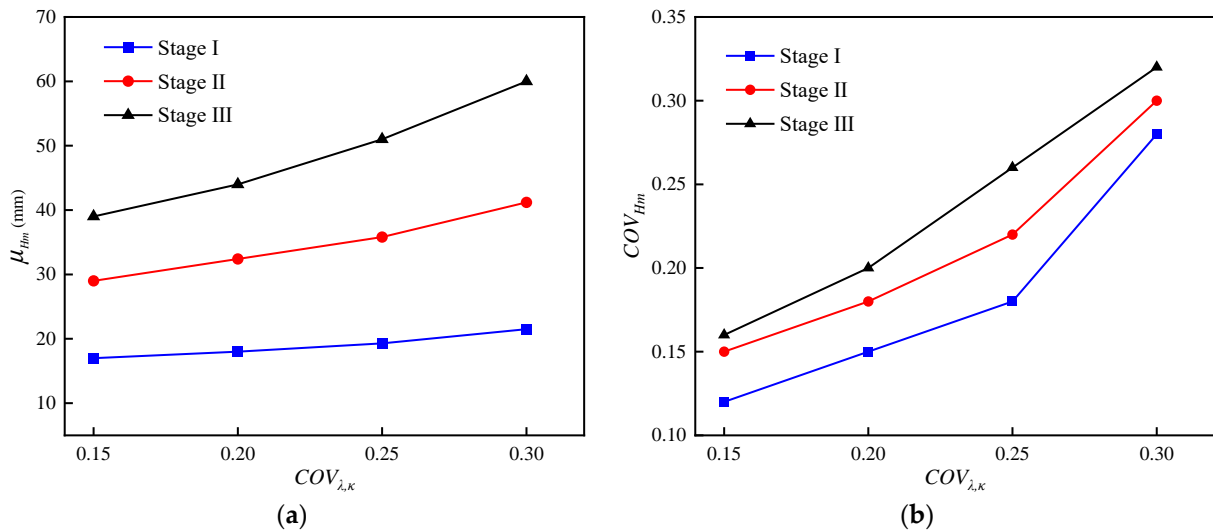


Figure 17. Effect of $COV_{\lambda,\kappa}$ on the ground surface settlement at various construction stages: (a) mean of H_m ; (b) COV of H_m .

Figure 18 presents the variable response of the PDF curves of the H_m and D'_m with the COV of MCC model parameters. With regard to the H_m , as shown in Figure 18a, it followed a log-normal distribution for all the investigated $COV_{\lambda,\kappa}$. The μ_{H_m} and σ_{H_m} increased with the increasing $COV_{\lambda,\kappa}$, and the peak of the PDF curve shifted to the right, indicating that the variation range became larger; thus, the COV_{H_m} increased accordingly, which corresponded to the results reflected in Figure 17. A closer inspection of the data shows the equivalence of the values of COV_{H_m} and $COV_{\lambda,\kappa}$. This observation was compatible with related studies [70], and the subtle discrepancy may be explained by the distinction between the single random variable approach and the random field variable approach. With regard to D'_m , as shown in Figure 18b, it also followed a log-normal distribution for all the investigated $COV_{\lambda,\kappa}$. The mean and standard deviation ($\mu_{D'_m}$ and $\sigma_{D'_m}$) generally increased with the increasing $COV_{\lambda,\kappa}$, and the COV of D'_m increased from 0.45 to 0.72, indicating a remarkable increase in dispersion. Besides, it is noticeable that the statistical characteristics were insignificantly different when the $COV_{\lambda,\kappa}$ were taken as 0.2 and 0.25, and their PDF curves were practically overlapped.

The relationship between the reliability index, β , and the $COV_{\lambda,\kappa}$ have also been investigated, as shown in Figure 19. With the increase of $COV_{\lambda,\kappa}$, the β reduced significantly from 2.7 to merely 0.1, which is virtually a linear decline. It can be learned that the variability of the deformation parameters of the MCC model has a considerable influence

on the reliability of the foundation settlement. It requires a thorough investigation to avoid underestimating COV, resulting in an overestimated reliability.

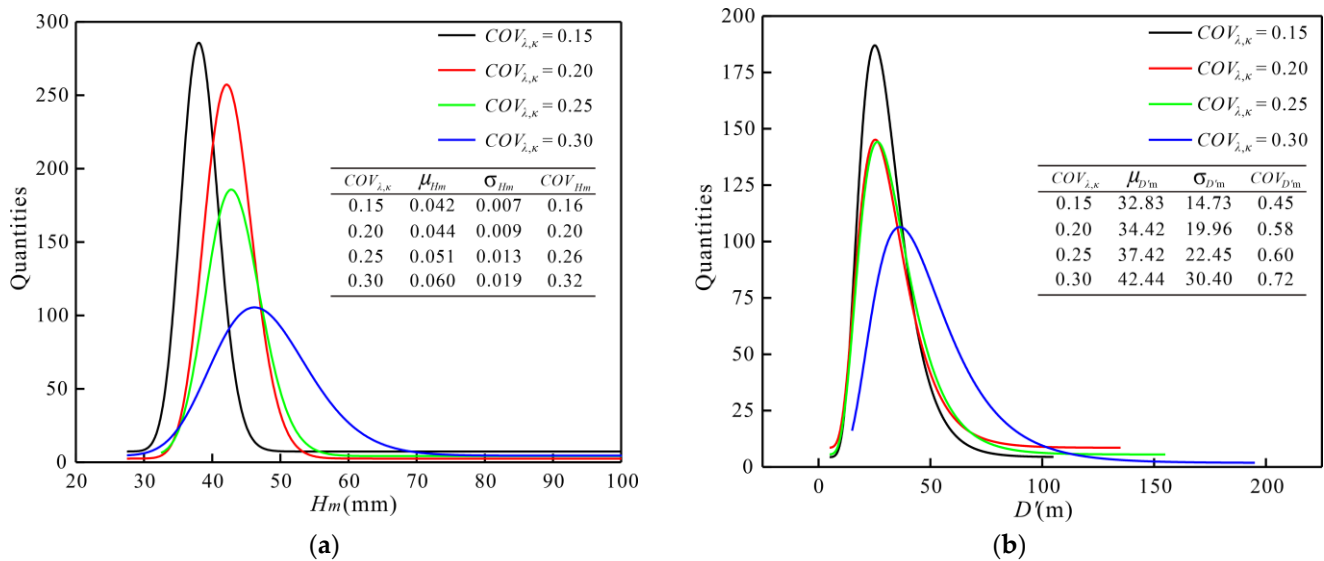


Figure 18. Effect of $COV_{\lambda,\kappa}$ on the PDF curves of probabilistic analysis of ground surface settlement of the excavation: (a) PDF of H_m ; (b) PDF of D'_m .

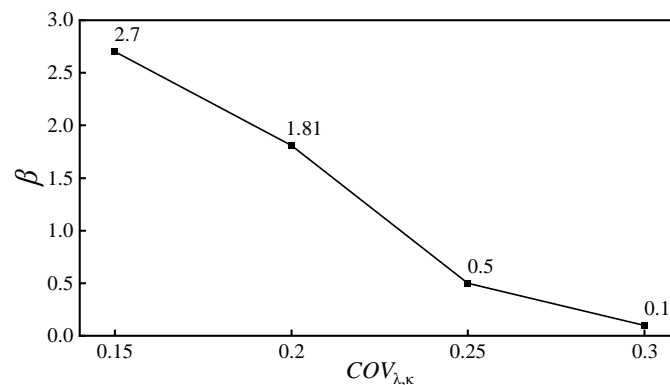


Figure 19. Reliability of ground surface settlement and $COV_{\lambda,\kappa}$.

5. Discussion

A strong relationship between MCC model parameters and deformation problems has been reported in the literature. A prior study examined the effect of MCC model parameters on the horizontal displacement at the front of the pier improved with drilled grouting piles, revealing a ranking according to the significance of the effect, namely, ν , λ , and M [71]. Several probabilistic analyses have also studied the effect of the spatial variability of κ and M on the bearing capacity of foundations [40] and the spatial variability of the individual parameter λ on the consolidation settlement of one-dimensional foundations [39]. However, previous studies have not brought up the results for the particular problem of ground surface settlement induced by embraced excavation. According to this study, for the braced excavation surface settlement caused by drawdown, the settlement is notably influenced by the deformation parameters of the MCC model (typically λ and κ). Both have a significant positive relationship, and κ plays a greater role than λ . This finding is inconsistent with previous studies, which have suggested that the effect of different parameters of the MCC model varies for a given engineering problem. A possible explanation can be stated as follows. The soil is initially in a limited state of elasticity. With the decline of the water table, the pore water pressure in the soil decreases, and the effective stress increases, which

is comparable to loading. However, the strain increment due to loading during this process was dominantly elastic. Therefore, the deformation parameter representing the elastic part, κ , has a greater impact than the parameter representing the plastic part, λ , during the deformation process.

The probabilistic analysis results of this study show that the H_m obtained from all realizations is within the range of 35–70 mm, which matches the range of $(0.10\% \sim 0.80\%)h_e$ (h_e denotes the excavation depth and is equivalent to 12 m herein) recorded by Wang et al. [72] in Shanghai area, China. In comparison, the analyzed values of D'_m are in a more extensive range of 5–110 m and are most centralized in the 20–35 m interval, more significant than the previously reported levels of $(0 \sim 1.0)h_e$ proposed by Hsieh and Ou [12]. This discrepancy may be due to the hydro-mechanical coupling effect under the drawdown action. Li et al. [73] also compared the settlement curves considering only excavation versus considering the coupling effect of excavation and draining by FEM analysis. They concluded that the location of the D'_m of the latter was remarkably greater than that of the former, even greater than twice.

With respect to surface settlement influence zoning, a horizontal overview of the current experience provides for two main categories. One category is h_e -related regulations; e.g., Hashash et al. [74] proposed that $(0 \sim 1)h_e$ is the primary influence zone, $(1 \sim 2)h_e$ is the secondary influence zone, and $(2 \sim 4)h_e$ is the minor influence zone. This regulation is analogous to the Shanghai technical specification for foundation pit engineering [75] and literature [12]. These regulations are applicable to scenarios considering only excavation, but it is debatable when considering draining scenarios. The other category is S_w -related regulations, e.g., the regulation for the Wuhan area proposed that $(0 \sim 3)S_w$ is the primary influence zone with a settlement of $(0.73 \sim 1)H_m$, $(3 \sim 10)S_w$ is the secondary influence zone with a settlement of $(0.45 \sim 0.73)H_m$, and $(10 \sim 30)S_w$ is the minor influence zone with a settlement of $(0.12 \sim 0.45)H_m$ [76]. While the technical specification for foundation pit support in the Shenzhen area provides that $(0 \sim 1)S_w$ is the primary influence zone, $(1 \sim 3)S_w$ is the secondary influence zone, and $(>3)S_w$ is the minor influence zone [77]. Thus, the zoning is regional empirical, and there is no unified theory for direct application. Based on the comparison with the settlement curves of the probabilistic analysis in this study, it is found that the influence range of settlement is independent of the spatial variability of the parameters, and the partitioning is more consistent with the principle of the literature [76].

It is quite puzzling that there is such a dramatic discrepancy between the Wuhan area and the Shenzhen area as mentioned above. It may be due to the close hydraulic connection between groundwater and surface water, such as the Yangtze River in the Wuhan area, with sufficient groundwater recharge and correspondingly greater funnel-shaped groundwater surface and consequently more excellent settlement coverage. In contrast, the Shenzhen area has a narrower river basin and less extensible stratigraphy, resulting in a narrower pumping area and settlement coverage. Hence, it is concluded that the influence range of draining and ground settlement are identical. For an excavation with a relatively homogeneous stratum, ground settlement is predominantly controlled by the drawdown. Meanwhile, the duration, volume, season of pumping, and the hydrogeological boundary of the excavation site also affect the shape of the depression cone formed by draining. In practical engineering, ground settlement is also related to the distribution of strata, compressibility, the thickness of the compressed layer, and surrounding buildings. To summarize, it is difficult to derive a universally applicable partitioning regulation, and it is required to integrate the above considerations.

There are still some issues for the study that requires to be examined in further research. Firstly, only two independent spatial variable parameters were taken as a random field in the study, but actually, there are more parameters (e.g., permeability, stiffness, strength, etc.) and scenarios could be expected to be taken into account as random variables in the realistic situation. The correlation between parameters can be modeled through the Copula approach [78,79] or other methods [80]. Secondly, this study addressed a simplified model without considering the complex stratigraphic sequence and varied hydraulic boundary

conditions. Practically, field-scale exploration and modeling technology have advanced dramatically currently [81]. Further studies can be implemented by refining the analytical model to explore the settlement pattern. Meanwhile, the unsaturated soil elastoplastic extended Cambridge principal model [82] can be introduced to perform the unsaturated hydro-mechanical coupling analysis during the draining and excavation.

6. Conclusions

The purpose of the current study was to investigate the effect of spatial variable MCC model parameters on the ground surface settlement reliability of a braced excavation during the entire draining, bracing, and excavating process. Employed an MCS-FORM hybrid approach, the uncertainties of the ground surface settlement and the location with the maximum settlement were analyzed, and the effect of the controlled standard threshold of surface settlement and COV of the parameters on the results were also investigated. The following conclusions can be drawn from the study:

- (1) The deformation parameters of the MCC models can be obtained from the laboratory oedometer test and corresponding empirical relation. Based on the sensitivity analysis, the surface settlement has a positive relationship with the parameters associated with compression and rebound deformation (λ and κ) of the MCC model, of which κ has a greater effect than λ .
- (2) The observed maximum settlement and the location with the maximum settlement of the probabilistic analysis follow a log-normal distribution. An increasing COV of parameters leads to an enhanced surface settlement, expansion of the significant influence region of settlement, and decreased reliability.
- (3) A comparison of the settlement between the deterministic and probabilistic results reveals that adopting the deterministic analysis for excavation surface settlement evaluation is capable of underestimating the risk due to the settlement and the significant influence region remarkably.
- (4) The reliability index is enhanced dramatically with the delimited controlled standard value of the surface settlement, H_{con} . It decreases significantly at the preliminary stage and then decreases progressively until stable during further excavating. Hence it is recommended to strengthen the settlement monitoring, particularly in the first two stages during construction.

To obtain more sophisticated observations, the further study enables to introduce more refined excavation analytical model with complex stratigraphic sequence and varied hydraulic boundary conditions, and considering more random variables and the correlation between variables. Meanwhile, the framework can be extended to perform the unsaturated hydro-mechanical coupling analysis by introducing perform the unsaturated hydro-mechanical coupling analysis.

Author Contributions: Conceptualization, S.Z. and H.C. (Hao Cheng); methodology, H.C. (Hui Chen); software, H.C. (Hui Chen) and H.J.; validation, S.Z. and X.L.; formal analysis, S.Z.; investigation, H.C. (Hui Chen) and H.J.; resources, H.C. (Hao Cheng); data curation, H.C. (Hao Cheng); writing—original draft preparation, H.C. (Hao Cheng) and H.J.; writing—review and editing, S.Z.; visualization, H.C. (Hui Chen); supervision, S.Z. and X.L.; project administration, H.C.; funding acquisition, H.C. (Hao Cheng) and S.Z. All authors have read and agreed to the published version of the manuscript.

Funding: This research was funded by the Research Project of China Railway Siyuan Survey and Design Group Co., Ltd. (No. 2020k158), National Natural Science Foundation of China (No. 42090055), Open Fund of Badong National Observation and Research Station of Geohazards (BNORSG202213), National Natural Science Foundation of China (Nos. 42072314, 41807271).

Institutional Review Board Statement: Not applicable.

Informed Consent Statement: Not applicable.

Data Availability Statement: Not applicable.

Conflicts of Interest: The authors declare no conflict of interest.

References

1. Zhang, W.; Han, L.; Gu, X.; Wang, L.; Chen, F.; Liu, H. Tunneling and Deep Excavations in Spatially Variable Soil and Rock Masses: A Short Review. *Undergr. Space* **2022**, *7*, 380–407. [[CrossRef](#)]
2. Gholampour, A.; Johari, A. Reliability-Based Analysis of Braced Excavation in Unsaturated Soils Considering Conditional Spatial Variability. *Comput. Geotech.* **2019**, *115*, 103163. [[CrossRef](#)]
3. Huang, X.; Schweiger, H.F.; Huang, H. Influence of Deep Excavations on Nearby Existing Tunnels. *Int. J. Geomech.* **2013**, *13*, 170–180. [[CrossRef](#)]
4. Zhang, W.; Liu, H. Basal Heave Stability. In *Design of Deep Braced Excavation and Earth Retaining Systems Under Complex Built Environment: Theories and Case Studies*; Zhang, W., Liu, H., Eds.; Springer: Singapore, 2022; pp. 9–49.
5. Terzaghi, K. *Theoretical Soil Mechanics*; Wiley: New York, NY, USA, 1943.
6. Skempton, A.W.; Bjerrum, L.A. Contribution to Settlement Analysis of Foundations on Clay. *Geotechnique* **1957**, *7*, 168–178. [[CrossRef](#)]
7. Wu, T.H.; Chang, N.Y.; Ali, E.M. Consolidation and Strength Properties of a Clay. *J. Geotech. Engrg. Div.* **1978**, *104*, 889–905. [[CrossRef](#)]
8. Pujades, E.; Vázquez-Suñé, E.; Carrera, J.; Jurado, A. Dewatering of a Deep Excavation Undertaken in a Layered Soil. *Eng. Geol.* **2014**, *178*, 15–27. [[CrossRef](#)]
9. Peck, R.B. Deep Excavation and Tunneling in Soft Ground. In *Proceedings of the 7th International Conference on Soil Mechanics and Foundation Engineering, State-of-the-Art-Volume*; State of the Art Report: Mexico City, Mexico, 1969; pp. 225–290.
10. Mana, A.I.; Clough, G.W. Prediction of Movements for Braced Cuts in Clay. *J. Geotech. Engrg. Div.* **1981**, *107*, 759–777. [[CrossRef](#)]
11. Ou, C.Y.; Hsieh, P.G.; Chiou, D.C. Characteristics of Ground Surface Settlement During Excavation. *Can. Geotech. J.* **1993**, *30*, 758–767. [[CrossRef](#)]
12. Hsieh, P.G.; Ou, C.Y. Shape of Ground Surface Settlement Profiles Caused by Excavation. *Can. Geotech. J.* **1998**, *35*, 1004–1017. [[CrossRef](#)]
13. Leung, E.H.Y.; NG, C.W.W. Wall and Ground Movements Associated with Deep Excavations Supported by Cast in Situ Wall in Mixed Ground Conditions. *J. Geotech. Geoenviron. Eng.* **2007**, *133*, 129–143. [[CrossRef](#)]
14. Wang, J.; Feng, B.; Liu, Y.; Wu, L.; Zhu, Y.; Zhang, X.; Tang, Y.; Yang, P. Controlling Subsidence Caused by De-watering in a Deep Foundation Pit. *Bull. Eng. Geol. Environ.* **2012**, *71*, 545–555. [[CrossRef](#)]
15. Indraratna, B.; Redana, I.W. Numerical Modeling of Vertical Drains with Smear and Well Resistance Installed in Clay. *Can. Geotech. J.* **2000**, *37*, 132–145. [[CrossRef](#)]
16. Shi, J.; Ng, C.W.W.; Chen, Y. Three-dimensional Numerical Parametric Study of the Influence of Basement Excavation on Existing Tunnel. *Comput. Geotech.* **2015**, *63*, 146–158. [[CrossRef](#)]
17. Liang, R.; Xia, W.; Feng, Y.; Jiang, G.; Liu, J. Simplified method for evaluating shield tunnel deformation due to adjacent excavation. *Tunn. Undergr. Sp. Tech.* **2018**, *71*, 94–105. [[CrossRef](#)]
18. Goh, A.T.C.; Zhang, R.; Wang, W.; Wang, L.; Liu, H.; Zhang, W. Numerical Study of the Effects of Groundwater Drawdown on Ground Settlement for Excavation in Residual Soils. *Acta Geotech.* **2020**, *15*, 1259–1272. [[CrossRef](#)]
19. Zou, Z.; Yan, J.; Tang, H.; Wang, S.; Xiong, C.; Hu, X. A Shear Constitutive Model for Describing the Full Process of the Deformation and Failure of Slip Zone Soil. *Eng. Geol.* **2020**, *276*, 105766. [[CrossRef](#)]
20. Cheng, H. Elastoplastic Constitutive Models for Unsaturated Soils with Finite Element Modeling and the Applications in Slope Deformation Analysis. Ph.D. Thesis, China University of Geosciences, Wuhan, China, 2019. (In Chinese).
21. Roscoe, K.H.; Schofield, A.N.; Thurairajah, A. Yielding of clays in states wetter than critical. *Geotechnique* **2015**, *13*, 211–240. [[CrossRef](#)]
22. Roscoe, K.H.; Burland, J.B. On the Generalized Stress-strain Behavior of Wet Clay. In *Engineering Plasticity*; Cambridge University Press: Cambridge, UK, 1968; pp. 535–609.
23. Borja, R.I.; Lee, S.R. Cam-clay plasticity, part 1: Implicit integration of elasto-plastic constitutive relations. *Comput. Methods Appl. Mech. Eng.* **1990**, *78*, 49–72. [[CrossRef](#)]
24. Xu, Z.; Wang, W. Selection of Soil Constitutive Models for Numerical Analysis of Deep Excavations in Close Proximity to Sensitive Properties. *Rock Soil Mech.* **2010**, *31*, 258–264. (In Chinese) [[CrossRef](#)]
25. Cassiani, G.; Brovelli, A.; Hueckel, T. A Strain-Rate-Dependent Modified Cam-Clay Model for the Simulation of Soil/Rock Compaction. *Geomech. Energy Environ.* **2017**, *11*, 42–51. [[CrossRef](#)]
26. Wang, L.; Zheng, G. Numerical Evaluation of the Upheave and Soil Arching Associated with Compaction Grouting in Shield Tunneling and Loading Process. *Tunn. Undergr. Sp. Tech.* **2022**, *128*, 104664. [[CrossRef](#)]
27. Gaone, F.M.; Doherty, J.P.; Gourvenec, S. An Optimization Strategy for Evaluating Modified Cam Clay Parameters Using Self-boring Pressuremeter Test Data. *Can. Geotech. J.* **2019**, *56*, 1668–1679. [[CrossRef](#)]
28. Negesa, A.B. Settlement Analysis of Pipe Culvert Situated in Soft Clay Treated with Prefabricated Vertical Drains. *Adv. Civ. Eng.* **2022**, *2022*, e9569077. [[CrossRef](#)]
29. Yao, Y.; Hou, W. Basic Mechanical Behavior of Soils and Their Elastoplastic Modeling. *Rock Soil Mech.* **2009**, *30*, 2881–2901. (In Chinese) [[CrossRef](#)]

30. Zdravković, L.; Taborda, D.M.G.; Potts, D.M.; Abadias, D.; Burd, H.J.; Byrne, B.W.; Gavin, K.G.; Houlsby, G.T.; Jardine, R.J.; Martin, C.M.; et al. Finite-Element Modelling of Laterally Loaded Piles in a Stiff Glacial Clay till at Cowden. *Géotechnique* **2020**, *70*, 999–1013. [[CrossRef](#)]
31. Lumb, P. The Variability of Natural Soils. *Can. Geotech. J.* **2011**, *3*, 74–97. [[CrossRef](#)]
32. Liu, X.; Ma, J.; Tang, H.; Zhang, S.; Huang, L.; Zhang, J. A Novel Dynamic Impact Pressure Model of Debris Flows and Its Application on Reliability Analysis of the Rock Mass Surrounding Tunnels. *Eng. Geol.* **2020**, *273*, 105694. [[CrossRef](#)]
33. Zhang, S.; Xiahou, Y.; Tang, H.; Huang, L.; Liu, X.; Wu, Q. Study on the Spatially Variable Saturated Hydraulic Conductivity and Deformation Behavior of Accumulation Reservoir Landslide Based on Surface Nuclear Magnetic Resonance Survey. *Adv. Civ. Eng.* **2018**, 7290640. [[CrossRef](#)]
34. Wang, C.; Osorio-Murillo, C.A.; Zhu, H.; Rubin, Y. Bayesian approach for calibrating transformation model from spatially varied CPT data to regular geotechnical parameter. *Comput Geotech.* **2017**, *85*, 262–273. [[CrossRef](#)]
35. Wu, T.H.; Gale, S.M.; Zhou, S.Z.; Geiger, E.C. Reliability of Settlement Prediction—Case History. *J. Geotech. Geoenviron. Eng.* **2011**, *137*, 312–322. [[CrossRef](#)]
36. Goh, A.T.C.; Kulhawy, F.H.; Wong, K.S. Reliability Assessment of Basal Heave Stability for Braced Excavations in Clay. *J. Geotech. Geoenviron. Eng. ASCE* **2008**, *134*, 143–153. [[CrossRef](#)]
37. Luo, Z.; DAS, B.M. System Probabilistic Serviceability Assessment of Braced Excavations in Clays. *Int. J. Geotech. Eng.* **2015**, *10*, 135–144. [[CrossRef](#)]
38. Zhang, R.; Goh, A.; Zhou, T.; Zhang, W. Reliability assessment of excavation-induced ground surface settlement with groundwater drawdown considering spatial variability. *J. Civ. Environ. Eng.* **2021**, *43*, 54–63. [[CrossRef](#)]
39. Lu, Z.; Zhang, M.; Guo, C. Reliability Analysis of Modified Cambridge Model Based on Stochastic Finite Elements Methods. *J. Shenyang Jianzhu Univ. (Nat. Sci.)* **2018**, *34*, 703–710. (In Chinese) [[CrossRef](#)]
40. Savvides, A.A.; Papadarakakis, M.A. Computational Study on the Uncertainty Quantification of Failure of Clays with a Modified Cam-Clay Yield Criterion. *SN Appl. Sci.* **2021**, *3*, 659. [[CrossRef](#)]
41. Abaqus. *ABAQUS User's Manual*, Version 6.13-EF; Hibbit, Karlsson & Sorensen Inc.: Providence, RI, USA, 2014.
42. Helweggs, S. *Applied Soil mechanics with ABAQUS Applications*; Wiley: New York, NY, USA, 2007.
43. Fenton, G.A.; Griffiths, D.V. Probabilistic Foundation Settlement on Spatially Random Soil. *J. Geotech. Geoenviron. Eng.* **2002**, *128*, 381–390. [[CrossRef](#)]
44. Zhu, H.; Zhang, L.M. Characterizing Geotechnical Anisotropic Spatial Variations Using Random Field Theory. *Can. Geotech. J.* **2013**, *50*, 723–734. [[CrossRef](#)]
45. China Railway Siyuan Survey and Design Group Co., Ltd. *Qinwang Channel (North Section) [YK1+680~YK2+706] Geotechnical Investigation Report*; China Railway Siyuan Survey and Design Group Co., Ltd.: Wuhan, China, 2021; p. 9.
46. Coleman, J.L.; Bolisetti, C.; Whittaker, A.S. Time-domain soil-structure interaction analysis of nuclear facilities. *Nucl. Eng. Des.* **2016**, *298*, 264–270. [[CrossRef](#)]
47. Forcellini, D.; Alzabeebee, S. Seismic fragility assessment of geotechnical seismic isolation (GSI) for bridge configuration. *Bull. Earthq. Eng.* **2021**, 1–22. [[CrossRef](#)]
48. Su, L.; Lu, J.; Elgamal, A.; Arulmoli, A.K. Seismic performance of a pile-supported wharf: Three dimensional finite element simulation. *Soil Dyn. Earthq. Eng.* **2017**, *95*, 167–179. [[CrossRef](#)]
49. Forcellini, D. The Role of the Water Level in the Assessment of Seismic Vulnerability for the 23 November 1980 Irpinia–Basilicata Earthquake. *Geosciences* **2020**, *10*, 229. [[CrossRef](#)]
50. GB/T 50123-2019. Standard for Geotechnical Testing Method. China Planning Press: Beijing, China, 2019. (In Chinese)
51. Phoon, K.K.; Kulhawy, F.H. Characterization of Geotechnical Variability. *Can. Geotech. J.* **1999**, *36*, 621–624. [[CrossRef](#)]
52. Baroth, J.; Malecot, Y. Probabilistic Analysis of The Inverse Analysis of An Excavation Problem. *Comput. Geotech.* **2009**, *37*, 391–398. [[CrossRef](#)]
53. Vanmarke, E.H. Probabilistic Modeling of Soil Profiles. *J. Geotech. Engrg. Div.* **1977**, *103*, 1227–1246. [[CrossRef](#)]
54. Liang, S.; Zhu, H. Statistical Analysis on Soil Indices of Lagoon Facies Soft Soil Layer in Hangzhou. *Subgrade Eng.* **2012**, *6*, 93–98. (In Chinese)
55. Li, X.; Xie, K.; Yu, Y. Research of the Characteristics of Correlation Distance on Soil Properties Indexes. *China Civil. Eng. J.* **2003**, *8*, 91–95. (In Chinese)
56. Li, X.; Hao, J. Orthogonal Test Design for Optimization of Synthesis of Super Early Strength Anchoring Material. *Constr. Build. Mater.* **2018**, *181*, 42–48. [[CrossRef](#)]
57. Li, Y.; She, L.; Wen, L.; Zhang, Q. Sensitivity Analysis of Drilling Parameters in Rock Rotary Drilling Process Based on Orthogonal Test Method. *Eng. Geol.* **2020**, *270*, 105576. [[CrossRef](#)]
58. Mukhopadhyay, A.; Dhawan, K. An L9 Orthogonal Design Methodology to Study the Impact of Operating Parameters on Particulate Emission and Related Characteristics During Pulse-jet Filtration Process. *Powder Technol.* **2009**, *195*, 128–134. [[CrossRef](#)]
59. Kumar, S.; Toan, C.D.; Vahedifard, F. Poisson's Ratio Characteristic Curve of Unsaturated Soils. *J. Geotech. Geoenviron. Eng.* **2021**, *147*, 04020149. [[CrossRef](#)]
60. McNeil, A.J.; Frey, R.; Embrechts, P. *Quantitative Risk Management: Concepts, Techniques, and Tools*; Princeton University Press: Princeton, NJ, USA, 2005.
61. Zhao, Y.G.; Ono, T. Moment Methods for Structural Reliability. *Struct. Saf.* **2001**, *23*, 47–75. [[CrossRef](#)]

62. Simões, J.T.; Neves, L.C.; Antão, A.N.; Guerra, N.M.C. Reliability assessment of shallow foundations on undrained soils considering soil spatial variability. *Comput. Nd Geotech.* **2020**, *119*, 103369. [[CrossRef](#)]
63. Gong, W.; Juang, C.H.; Martin, J.R.; Tang, H.; Wang, Q.; Huang, H. Probabilistic Analysis of Tunnel Longitudinal Performance Based upon Conditional Random Field Simulation of Soil Properties. *Tuun. Undergr. Sp. Tech.* **2018**, *73*, 1–14. [[CrossRef](#)]
64. ISO 2394. General Principles on Reliability for Structures. 2nd ed. ISO: Geneve, Switzerland, 1998.
65. Gudipati, V.K.; Cha, E.J. Target Reliability Index Optimization Framework for Multiple Building Classes Based on Community-Level Objectives. *Struct. Saf.* **2021**, *91*, 102097. [[CrossRef](#)]
66. Shen, X. A Technique Research on Maintaining the Foundationpit of the Large Passenger Railway Station. Master's Thesis, Zhejiang University, Hangzhou, China, 2011. (In Chinese)
67. Wang, Y. Research on the Deformation Law and Optimal Design of the Deep Foundation Pit Support Structure in the Silt Soft Soil Area of Hangzhou. Master's Thesis, Xi'an University of Architecture and Technology, Xi'an, China, 2020. (In Chinese) [[CrossRef](#)]
68. Qin, S. Study on Stability Law of Deep Foundation Pit in Hangzhou Metro. Master's Thesis, Taiyuan University of Technology, Taiyuan, China, 2019. (In Chinese) [[CrossRef](#)]
69. Wei, G.; Hua, X.; Yu, X. Construction Monitoring analysis of deep foundation pit excavation of a metro station in Hangzhou. *Eng. J. Wuhan Univ.* **2016**, *49*, 917–923+936. (In Chinese) [[CrossRef](#)]
70. Zhang, S.; Zhong, L.; Xu, Z. Reliability of Foundation Pile Based on Settlement and a Parameter Sensitivity Analysis. *Math. Probl. Eng.* **2016**, *2016*, e1659549. [[CrossRef](#)]
71. Zhang, Y. Effects of Parameters of Modified Cambridge Model on Computed Results. *Rock Soil Mech* **2006**, *27*, 441–444. (In Chinese) [[CrossRef](#)]
72. Wang, J.; Xu, Z.; Wang, W. Wall and Ground Movements Due to Deep Excavations in Shanghai Soft Soils. *J. Geotech. Geoenviron. Eng.* **2010**, *136*, 985–994. [[CrossRef](#)]
73. Li, F.; Chen, G.; Liu, X. Deformation characteristics of suspended curtain deep foundation pit of metro lines. *Chin. J. Geotech. Eng.* **2018**, *12*, 2182–2190. [[CrossRef](#)]
74. Hashash, Y.M.A.; Osouli, A.; Marulanda, C. Central Artery/tunnel Project Excavation Induced Ground Deformations. *J. Geotech. Geoenviron. Eng.* **2008**, *134*, 1399–1406. [[CrossRef](#)]
75. DG/TJ 08-61-2018. Technical Code for Excavation Engineering. Shanghai Municipal Housing and Urban-Rural Development Management Committee: Shanghai, China, 2018. (In Chinese)
76. DB42/T 159-2012. Technical Specification for Excavation Engineering. Hubei Provincial Department of Housing and Urban-Rural Development: Wuhan, China, 2012. (In Chinese)
77. SJG 05-2011. Technical Code for Retaining and Protection of Excavations in Shenzhen City. China Architecture & Building Press: Beijing, China, 2020. (In Chinese)
78. Pan, Y.; Zhang, L.; Wu, X.; Qin, W.; Skibniewski, M.J. Modeling face reliability in tunneling: A copula approach. *Comput. Geotech.* **2019**, *109*, 272–286. [[CrossRef](#)]
79. Ng, C.W.W.; Qu, C.; Cheung, R.W.M.; Guo, H.; Ni, J.; Chen, Y.; Zhang, S. Risk assessment of soil slope failure considering copula-based rotated anisotropy random fields. *Comput. Geotech.* **2021**, *136*, 104252. [[CrossRef](#)]
80. Xiahou, Y.; Zhang, S.; Tang, H.; Liu, X.; Wu, Q. Study of Structural Cross-constraint Random Field Simulation Method Considering Spatial Variation Structure of Parameters. *Rock Soil Mech.* **2019**, *40*, 4935–4945. (In Chinese) [[CrossRef](#)]
81. Wang, J.; Schweizer, D.; Liu, Q.; Su, A.; Hu, X.; Blum, P. Three-Dimensional Landslide Evolution Model at the Yangtze River. *Eng. Geol.* **2021**, *292*, 106275. [[CrossRef](#)]
82. Cheng, H.; Tang, H.; Wu, Q.; Lei, G. An Elasto-plasticity Extended Cam-clay Model for Unsaturated Soils Using Explicit Integration Algorithm in FEM with Hydraulic Hysteresis. *Rock Soil Mech.* **2020**, *41*, 676–686. (In Chinese) [[CrossRef](#)]